

Improvement of Low-dose MDCT Images by Applying a Novel Adaptive Median Filter with Local Averaging

Jiehang Deng*, Koichiro Hiratsuka¹, Tomokazu Ishida², Haruhiko Shirai³, Jousuke Kuroiwa³, Tomohiro Odaka³, and Hisakazu Ogura³

¹University of Fukui at Fukui, Information Center, JAPAN

²University Hospital, University of Fukui at Fukui, Department of Radiology, JAPAN

³University of Fukui at Fukui, Faculty of Graduate School of Engineering, JAPAN

Received Date: 15 March 2009, Accepted Date: 29 April 2009

Abstract

In order to reduce the quantum noise level without the expense of feature preservation of small tumors, a novel 3D adaptive median filter with local averaging is developed according to the size of tumors and the distribution of voxel value in a local region. In this paper, two new methods based on entropy of correlation and mutual information of correlation are also proposed to evaluate the validity and efficiency of the proposed filter quantitatively. The proposed filter is applied to processing low-dose abdominal datasets, and experimental results show that the filtering technique is able to reduce the level of the quantum noise and preserve the features of the edge region and the shape of the tumors for low-dose abdominal 3D MDCT images.

images with different filters. However, only the general filtering procedures were shown in their studies, without a description of the detailed structure or the basis of the parameters.

Kachelrieb et al. proposed multi-dimensional adaptive filtering for low-dose CT images [12]. Yang et al. [13] and Yasuda et al. [14] improved the low-dose CT images by using wavelet transform. Suzuki et al. [3] applied neural filter to improving the low-dose angiogram sequences. These specific methods aimed at achieving effective trade-offs between smoothing efficiency, feature preservation over the whole image or the entire 3D dataset. However, it is paramount to discern tumors of less than 5 mm, preferably down to 2 mm in diameter, and determine their size for radiologists. Therefore, how to design filtering and evaluating methods for reducing the quantum noise according to the size and the distribution of voxel value of small regions being suspected of tumors is a serious issue.

In 2005, Chan et al. [15] applied an adaptive median-type filter to remove salt-and-pepper noise with a noise level as high as 90%. However, the quantum noise is different from the impulse noise due to quantum fluctuations [16]. The correlation of quantum noise in direction of the Z axis is weak in comparison with that of the XY plane. Therefore, we extend the 2D adaptive median filter to 3D. To reduce the quantum noise with the effect of the feature preservation of small tumors, we propose the adaptive local averaging strategy according to the size and the distribution of voxel value of the small region being suspected of tumors. In this paper the quantum noise in low-dose abdominal MDCT images are reduced by the novel 3D adaptive median filter with local averaging. Local histograms, voxel value profiles and several image quality assessment indices are applied to evaluating the validity and efficiency of this filtering technique.

Besides, Wang and Bovik [17] proposed a universal image quality index Q to evaluate the natural image under consideration of voxel value correlation in a small region in 2002. In

2004, they modified Q to propose a new image quality index, i.e., MSIMM [18]. In 2008, another group of researchers Wang and Ma [19] proposed a statistical method to evaluate natural and medical volume data by combining the strategy of Q. All these new image quality indices are designed without consideration of the voxel value correlation in different directions of a small region. To alleviate this limitation, two new indices based on entropy of correlation and mutual information of

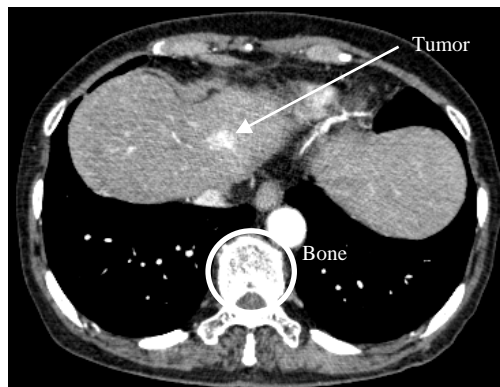


Figure 1. Body region.

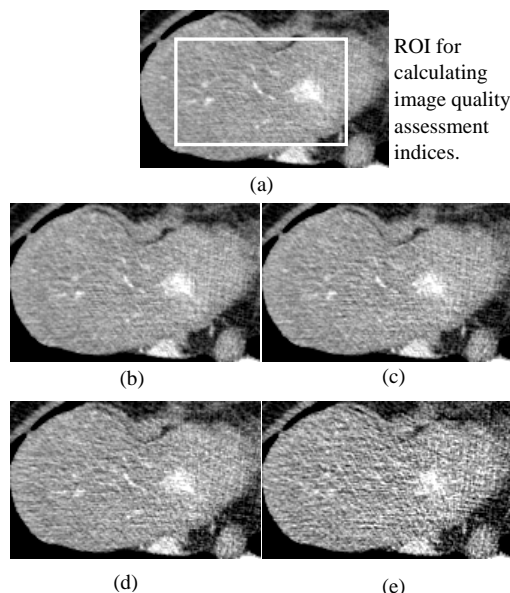


Figure 2. Liver region of MDCT images (Slice 15). (a) Normal-dose image. (b-e) 80%, 60%, 40% and 20%-dose images.

correlation are developed to assess the filtering performance in directions of X , Y , and Z axis.

2. MATERIAL AND METHODS

Data Collection

By using a 16-row MDCT system (Sensation 16; SIEMENS), we perform helical scanning under the following scan conditions: tube voltage of 120 kV, tube current of 220 mA, scan time of 0.5 sec/rotation, image slice thickness of 0.75 mm, slice interval of 0.75 mm, and field of view of 384 mm with a reconstruction function of B31f. The helical pitch is 0.75. Volume helical scan time for the examination is 12 s. The X-ray dose changes automatically in response to patient body thickness using an auto exposure control mechanism.

For raw data, the X-ray dose received in an ordinary routine examination is assigned 100% (i.e., normal-dose). The dose is decreased to 80%, 60%, 40% and 20%. Image reconstruction is then performed to create the low-dose images. In comparison with the normal ones, i.e., normal-dose images, a large amount of quantum noise distributes randomly on every slice of low-dose images. The noise level increases with the decreasing radiation dose as shown in Figures 1 and 2. The region of interest (ROI) for calculating image quality assessment indices are indicated by the white rectangle in Figure 2(a).

3D Adaptive Median Filter with Local Averaging

In this paper, the adaptive median technique is extended to 3D by changing the 2D filtering window to a local region R_{xyz}^n which is defined as follows:

$$R_{xyz}^n = \{(x', y', z') \mid (x'-x)^2 + (y'-y)^2 + (z'-z)^2 \leq r_n^2\}$$

where r_n is the radius of the n th neighbors whose origin is at the point (x, y, z) , e.g., $r_1^2=1$, $r_2^2=2$, and so on. We refer 3D adaptive median filter as 3D AM hereafter.

Let us denote that n_{max} is the maximum order of neighbors, and v_{xyz} is the current voxel value at (x, y, z) . The 3D AM based on the 2D adaptive

median filter (2D AM) [15] identifies and replaces noise candidates with the median value in R_{xyz}^n .

To reduce the quantum noise level without expense of feature preservation of small tumors, we introduce the adaptive local averaging strategy into the 3D AM according to the size of small tumors and the distribution of voxel value in a local region. The 3D adaptive median filter with local averaging (3D AMLA) is carried out as follows:

- (1) Initialize the order of neighbors $n = 1$.
- (2) Compute S_{xyz}^{min,R^n} , S_{xyz}^{med,R^n} and S_{xyz}^{max,R^n} , which are the minimum, median, and maximum values with adaptive local averaging in R_{xyz}^n , respectively.
- (3) If $S_{xyz}^{min,R^n} < S_{xyz}^{med,R^n} < S_{xyz}^{max,R^n}$, go to step 5; otherwise, the values of current voxel neighborhood are almost the same, e.g., the current voxel is in air region of lungs or intro regions of a liver. Then the size of this neighborhood needs to be enlarged to identify noise candidates, further. Therefore, set $n = n + 1$.
- (4) If $n < n_{max}$, go to step 2; otherwise, replace v_{xyz} with S_{xyz}^{med,R^n} .
- (5) If $S_{xyz}^{min,R^n} < v_{xyz} < S_{xyz}^{max,R^n}$, then v_{xyz} is kept unchanged; otherwise, v_{xyz} is replaced by S_{xyz}^{med,R^n} .

To calculate S_{xyz}^{min,R^n} , S_{xyz}^{med,R^n} , and S_{xyz}^{max,R^n} , the voxel values in the local region R_{xyz}^n are sorted in an increasing order, saved in an array with one dimension, and denoted as $A = \{v_i \mid i=1, 2, \dots, M\}$, where v_i is the i th voxel value in the

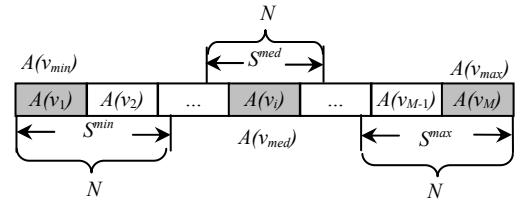


Figure 3. Schematic diagram of the sorted array in local region R_{xyz}^n , i.e.

$$A(v_i), i = 1, \dots, M.$$

array and M is the size of R_{xyz}^n . Let us denote $A(v_{min})$, $A(v_{med})$ and $A(v_{max})$ as the minimum, median and maximum in A , respectively. We prepare three sets, S^{min} , S^{med} and S^{max} . S^{min} and S^{max} are the first and last N elements of A , respectively. S^{med} is N elements centered around $A(v_{med})$. The schematic diagram is shown in Figure 3.

The local distribution of voxel values in $\{A(v_1), A(v_2), \dots, A(v_M)\}$ can be divided into three types:

$$\begin{aligned} type = 1, & A(v_{min}) \ll A(v_{med}) < A(v_{max}); \\ type = 2, & A(v_{min}) \leq A(v_{med}) \leq A(v_{max}); \\ type = 3, & A(v_{min}) < A(v_{med}) \leq A(v_{max}). \end{aligned} \quad (1)$$

where $type$ represents the type of local distribution.

For $type = 1$, the voxels in S^{min} would have high probability as noise candidates. Therefore, S_{xyz}^{min,R^n} is set as the median value of S^{min} . S_{xyz}^{med,R^n} and S_{xyz}^{max,R^n} are decided by the average values of S^{med} and S^{max} , respectively. Similarly, S_{xyz}^{max,R^n} is set as the median value of S^{max} . S_{xyz}^{min,R^n} and S_{xyz}^{med,R^n} are set as the average values of S^{min} and S^{med} in the case of $type = 3$.

For $type = 2$, noise candidates could appear in both S^{min} and S^{max} . Accordingly, S_{xyz}^{min,R^n} , S_{xyz}^{med,R^n} , and S_{xyz}^{max,R^n} are all set as the averages of S^{min} , S^{med} , and S^{max} .

The 3D AMLA can change the size of local region if the voxel values inside are almost the same, that is, $S_{xyz}^{min,R^n} = S_{xyz}^{med,R^n} < S_{xyz}^{max,R^n}$ or $S_{xyz}^{min,R^n} < S_{xyz}^{med,R^n} = S_{xyz}^{max,R^n}$ or $S_{xyz}^{min,R^n} = S_{xyz}^{med,R^n} = S_{xyz}^{max,R^n}$. Voxels whose values are not inside the open interval $(S_{xyz}^{min,R^n}, S_{xyz}^{max,R^n})$ are considered as noise candidates, and will be replaced by S_{xyz}^{med,R^n} . Because of the application of adaptive local averaging strategy, the value interval of normal voxel, i.e., $(S_{xyz}^{min,R^n}, S_{xyz}^{max,R^n})$, has been shrunk, and the features can be

preserved in comparison to 3D AM. Therefore, quantum noise candidates can be detected and replaced effectively by 3D AMLA without compromising the quality of diagnostic images.

Image Quality Assessment Indices

We evaluate the image quality by several indices. Each value of the indices is described as follows:

Standard deviation:

$$SD = \sqrt{\frac{\sum_{v \in R} (v - \bar{v})^2}{N_R}} \quad (2)$$

Uniformity:

$$UM = \sum_{m=0}^{N_B-1} p_B(m)^2 \quad (3)$$

Entropy:

$$ET = - \sum_{m=0}^{N_B-1} p_B(m) \log_2 p_B(m), \quad (4)$$

Mutual information:

$$MI = - \sum_{m=0}^{N_B-1} \sum_{m'=0}^{N_B-1} p_B(m, m') \log_2 \frac{p_B(m, m')}{p_B(m) p_B(m')} \quad (5)$$

Divergence:

$$DV = \sum_{m=0}^{N_B-1} p_B(m) \log_2 \frac{p_B(m)}{p'_B(m)} \quad (6)$$

where

$$\begin{aligned} p_B(m) &= \sum_{v=CT_{min}+m \times B_s-1}^{CT_{max}+(m+1) \times B_s} p(v) \quad (v \in \Phi_{CT}), \\ p_B(m, m') &= \sum_{v=CT_{min}+m \times B_s-1}^{CT_{min}+(m+1) \times B_s} \sum_{v'=CT_{min}+m' \times B_s-1}^{CT_{min}+(m'+1) \times B_s} p(v, v'), \\ p(v) &= \frac{N_v}{N_R} \quad (v \in \Phi_{CT}), \end{aligned}$$

$$\Phi_{CT} \in [CT_{min}, CT_{max}],$$

v is a voxel value in a dataset. m is a bin index where v is located in the histogram. v' and m' are the voxel value and index in a reference dataset. R is a voxel set inside ROI (Figure 2(a)) in all slices of a 3D dataset. \bar{v} and N_R are the mean value and the voxel number in the

ROI. N_v is the number of voxel whose value is v . N_B is bin number. B_s is bin size, i.e., the number of voxel values inside a bin. $p_B(m)$ is the percentage of CT value in the m th bin while $p'_B(m)$ is the percentage in a reference dataset corresponding to $p_B(m)$, as shown in Figure 4(b). $p(v)$ is the percentage of CT value v inside ROI; Φ_{CT} is the integer interval of CT value. CT_{min} and CT_{max} are the minimum and maximum of CT value. In this paper, CT_{min} and CT_{max} are $-1024, 3071$ HU, respectively.

To evaluate the distribution of small regions through ET, UM, MI and DV , the interval of CT value is divided into N_B bins with the same size B_s as shown in Figure 4. In Figure 4(a), the radius of a small region being suspected of a tumor is about 1 voxel in corresponding to 7 voxels whose values should be very close on the basis of the continuity of the attenuation value of the tumor. These 7 voxels generally include 4 kinds of continuous attenuation value. Therefore the bin size B_s is set at 4 HU (i.e., bin number N_B is equal to 1024) to calculate the distributions.

In evaluating the image quality, it is important to calculate the correlation of adjacent voxels in different directions. We employ entropy and mutual information calculated from the joint distributions of each voxel and its first neighbors in each direction of X, Y , or Z axis through dividing the CT interval Φ_{CT} into N_B bins. The entropy and mutual information are referred as entropy of correlation (EC) and mutual information of correlation (MIC), respectively. EC and MIC are given as follows.

Entropy of correlation:

$$EC(d) = - \sum_{m, m^d \in R} p_B(m, m^d) \log_2 p_B(m, m^d) \quad (7)$$

Mutual information of correlation:

$$MIC(d) = - \sum_{m=0}^{N_B-1} \sum_{m^d=0}^{N_B-1} p_B(m, m^d) \log_2 \frac{p_B(m, m^d)}{p_B(m) p'_B(m^d)} \quad (8)$$

where

$$p_B(m, m^d) = \sum_{v=CT_{min}+m \times S_B-1}^{CT_{min}+(m+1) \times S_B} \sum_{v^d=CT_{min}+m^d \times S_B-1}^{CT_{min}+(m^d+1) \times S_B} p(v, v^d),$$

v^d is the first neighbor of v in the direction of d (i.e., $d = X, Y$, or Z axis); similarly, m and m^d denote bin indexes where the v and v^d are located. EC and MIC reflect a degree of correlation and similarity of adjacent voxels, respectively.

All quantities of the indices are calculated within the ROI because our aim in filtering is to focus on the intra-hepatic tumors.

3. EXPERIMENTS

Filtering experiments

The low-dose 3D abdominal images are filtered by using 2D AM, 3D AM and 3D AMLA as depicted in Figure 5. For 3D AMLA, to determine the type of local distribution of voxel value in local region R_{xyz}^n , the line l in Figure 6(a) is calculated according to $A(v_{min})$ and $A(v_{max})$. Let us denote Δ_i as the difference between $A(v_i)$ and the corresponding point on the line l , i.e., $\Delta_i = A(v_i) - l(i)$. The three types in Eq. (1) are decided numerically as follows:

- $type = 1$, if $\Delta_i > 0$, for all $i = 2, \dots, M-1$;
- $type = 3$, if $\Delta_i < 0$, for all $i = 2, \dots, M-1$; (9)
- $type = 2$ otherwise.

The schematic diagram of calculating different types of local distribution of voxel value is shown in Figure 6(a). To show the effectiveness of this classifying, the voxel value of $type = 1, 2$ and 3 are represented by different colors in the liver region (Figure 2(b)), as shown in Figure 6(b). The boundaries and the intro-region of the liver can be

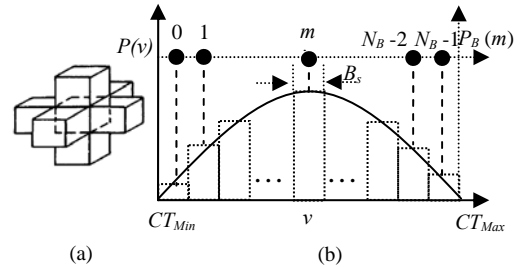


Figure 4. Schematic diagram of a small region in the case of that the radius is 1 voxel(a), and a distribution of CT value in N_B bins with the same bin size B_s (b).

recognized well in Figure 6(b). Therefore, 3D AMLA could reduce the noise level adaptively according to the different types.

On the other hand, radiologists must recognize the tumors whose size is even around 5 mm, preferably down to 2 mm (i.e., 2–3 voxels in diameter). Hence, it is vital that the filtering

method must be developed according to this requirement. To this end, N (the size of three sets: S^{min} , S^{med} and S^{max}) is set at 3. The parameter value of the maximum order of neighborhood n_{max} is defined as 9 through several experiments. N and n_{max} will be changed if spatial resolution of MDCT images is changed.

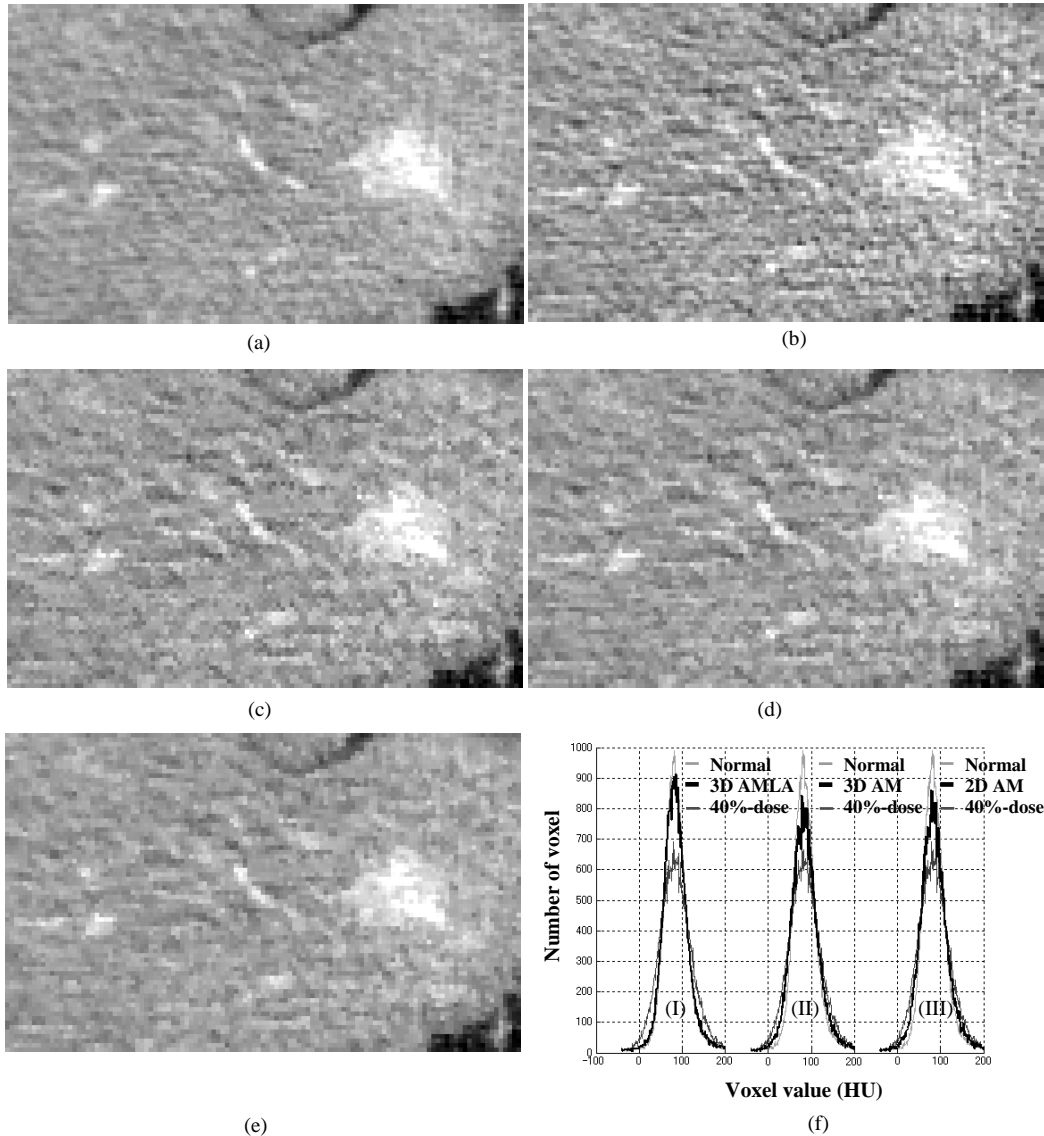


Figure 5. Tumor region from different datasets in the 15th slice and the local histograms in ROI. (a-b) Normal and 40%-dose images. (c-e) Results filtered by 2D AM, 3D AM and 3D AMLA. (f) Local histogram of (a-e). (f)-(I), (f)-(II) and (f)-(III) depict the local histograms of 3D AMLA, 3D AM and 2D AM, respectively.

Qualitative Evaluations

The results filtered by different methods described in this paper are shown in Figure 5. In addition, local histograms and voxel value profiles are applied in evaluating the filtering performance in detail.

The ROI of the normal dose image is shown in Figure 5(a). The noise level around the edge of the tumor indicated by the arrow in Figure 1 has been reduced smoothly without much disturbance from the noise in the filtered results of 3D AM in comparison with the low-dose images and results obtained by 2D AM, as shown in Figures 5(b-d). On the other hand, the voxel value profiles of original and filtered datasets are shown in Figure 7. The locations for extracting voxel values to construct profiles are indicated by 3 lines on the anatomical sections of the low-dose dataset as shown in Figure 7(a). Voxel profiles of the transversal, sagittal and coronal sections are depicted in Figures 7(b-d). In comparison to the profiles of normal ones, the peaks indicated by dotted circles are considered as noise candidates, while the peaks indicated by dotted squares are considered as subtle information. As shown in the profiles of the sagittal section in Figure 7(c), the noise candidates indicated by the dotted circles remain almost unchanged after being filtered by 2D AM, but they are removed in the filtered results of 3D AM.

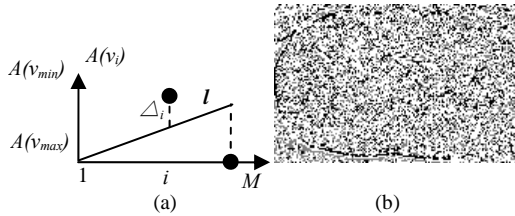


Figure 6. Different types of local distribution in R^3 . (a) A schematic diagram of calculating different types of local distribution. (b) The diagram of different types in the part of the liver region shown in Figure 2(b). The black pixels represent *type = 1*, white *type = 2* and gray *type = 3*, respectively.

Direct observations and voxel value profiles show that the correlation of internal organs in direction of Z axis is effectively used to reduce the quantum noise in 3D AM in comparison to 2D AM.

In Figures 5(a), (c) and (d), in comparison to 3D AM, the shape and the voxel value of the tumor in results obtained by 3D AMLA are closer to those of the normal ones. The local histogram of 3D AMLA (Figures 5(f)-(I)) almost overlaps with the one of normal-dose images, whereas 3D AM (Figure 5(f)-(II)) and 2D AM (Figure 5(f)-(III)) can not achieve this good performance. The 3D AMLA improve the local histogram greatly in comparison with 2D and 3D AM. Furthermore, the noise candidates indicated by the dotted circles (Figures 7 (b) and (d)) are detected and replaced only partially by 2D and 3D AM, while they almost completely vanish after being filtered by 3D AMLA. The most importance is that the subtle intensity indicated by the dotted squares and the tumor size are retained well in the filtered results of 3D AMLA. Therefore 3D AMLA is efficient to reduce the quantum noise and achieves the best trade-offs between smoothing effect and feature preservation.

Quantitative Evaluations

The noise level of the filtered results is reduced and close to that of the normal-dose images, which is evaluated by SD in Table 1. In addition, with the decreasing dose level, ET and UM of the low-dose images become far from those of the normal ones; DV between normal and low-dose images decrease; MI becomes large; the proposed EC and MIC decreases. It indicates that the ET , UM , MI , DV , EC and MIC work well to reflect the variation degree of the feature preservation.

In Table 1, the variations of the index values show that image qualities of the filtered results are improved and close to the normal ones. The difference values of the indices between normal-dose images and the results filtered by 3D AMLA are smaller than those filtered by 3D and 2D AM. In particular, it can be demonstrated by using EC and MIC that the

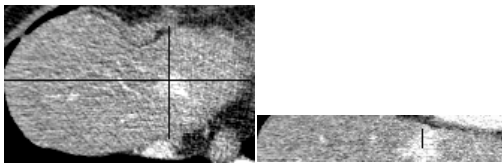
Table 1. Quantitative results. *SD, ET, UM, DV, MI, EC* and *MIC* denote the standard deviation, entropy, uniformity, divergence, mutual information, entropy of correlation and mutual information of correlation, respectively.

	Unfiltered datasets				Filtered datasets (40%-dose)			
	20%-dose	40%-dose	60%-dose	80%-dose	Normal dose	3D AMLA	3D AM	2D AM
<i>SD</i>	56.2	43.8	39.2	36.8	34.7	35.5	38.3	38.1
<i>ET</i>	5.84	5.43	5.23	5.08	4.96	5.03	5.19	5.18
<i>UM</i>	0.0214	0.0293	0.0346	0.0389	0.0429	0.0404	0.0356	0.0359
<i>DV</i>	0.452	0.148	0.048	0.012	--	0.007	0.0380	0.0349
<i>MI</i>	0.42	0.69	1.06	1.58	--	0.72	0.70	0.66
<i>EC (X)</i>	339	603	831	1046	1263	1195	956	920
<i>EC (Y)</i>	299	533	727	915	1101	1071	859	877
<i>EC (Z)</i>	250	444	603	758	916	893	702	646
<i>MIC (X)</i>	0.43	0.50	0.58	0.65	0.71	0.70	0.61	0.56
<i>MIC (Y)</i>	0.24	0.31	0.37	0.43	0.49	0.53	0.44	0.46
<i>MIC (Z)</i>	0.21	0.25	0.30	0.36	0.41	0.47	0.38	0.30

degree of correlation and similarity of adjacent voxels in all directions in the results filtered by 3D AMLA are closer to the normal ones than those obtained by 2D AM and 3D AM.

In order to show further effective performance of 3D AMLA, quantitative results of datasets

filtered by 3D AMLA with different dose level are shown in Table 2. According to Table 2, noise level has been reduced effectively (as *SD* shows). The filtered datasets close to normal dose images (as *ET, UM, DV* and *MI* show) in the degree of small regions which are



Transversal and sagittal sections. Coronal section.

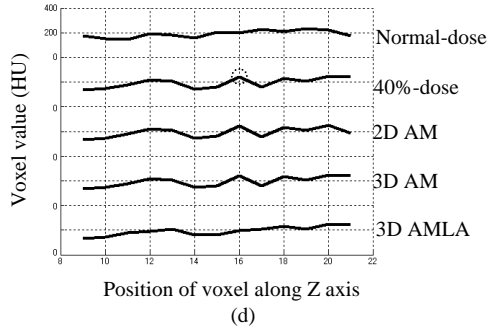
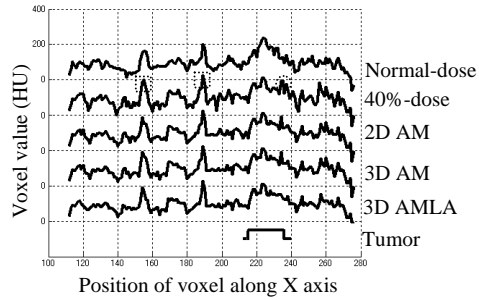
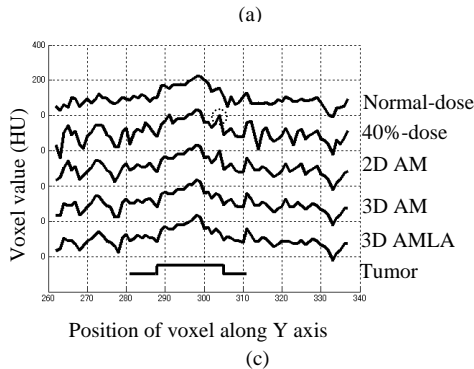


Figure 7. Voxel value profiles from different anatomical sections. (a) Extracting position of the profiles indicated by the black lines. (b-d) Voxel value profiles of transversal, sagittal and coronal sections.

Table 2. Quantitative results of datasets filtered by 3D AMLA with different dose level (Normal dose is for reference).

	20%- dose	40%- dose	60%- dose	80%- dose	Normal dose
<i>SD</i>	42.2	35.5	33.4	32.1	34.7
<i>ET</i>	5.37	5.03	4.88	4.77	4.96
<i>UM</i>	0.0307	0.0404	0.0461	0.0504	0.0429
<i>DV</i>	0.114	0.007	0.008	0.025	--
<i>MI</i>	0.48	0.72	0.96	1.21	--
<i>EC (X)</i>	712	1195	1551	1865	1263
<i>EC (Y)</i>	642	1071	1386	1661	1101
<i>EC (Z)</i>	535	893	1153	1387	916
<i>MIC (X)</i>	0.57	0.70	0.80	0.88	0.71
<i>MIC (Y)</i>	0.41	0.53	0.61	0.68	0.49
<i>MIC (Z)</i>	0.36	0.47	0.54	0.61	0.41

suspected of small tumors. Moreover, values of *EC* and *MIC* in directions of *X*, *Y* and *Z* axis confirm the correlation in the small regions of filtered datasets close to the normal dose images in these directions. For example, *EC* and *MIC* of the filtered datasets of 40%-dose images are nearly the same to the ones of the normal dose images in different directions. It further indicates that 3D AMLA performs effectively to improve the image quality of low-dose images. The dose level can be reduced to a large degree after performing 3D AMLA.

4. DISCUSSION

Since MDCT is a 3D imaging modality, the correlation in all 3D directions should be used to improve the image quality. The quantum noise is widely distributed throughout the projection data, and especially its correlation along the direction of *Z* axis is weak. Therefore, 2D AM should be extended to 3D for reducing the quantum noise by using the correlation of internal organs in 3D. In addition, noises around a tumor should not be smoothed while the tumor edges are blurred. Therefore, the adaptive local averaging strategy aiming to preserve edges and shape of small regions (Figure 4(a)) which are suspected of tumors is applied to designing the 3D AMLA. In 3D AMLA, finally, the quantum noise level can be reduced with the effect of feature preservation of small tumors.

In this paper, several image quality indices (*SD*, *ET*, *UM*, *DV*, *MI*, *EC* and *MIC*) are computed to evaluate the feature preservation. In Table 1, *EC* in all directions decreases with X-ray dose level. It indicates that the correlation of adjacent voxels is degraded with a decrease in dose level. In addition, the similarity of adjacent voxels becomes low when the dose level decreases as illustrated by *MIC*. With the decreasing correlation and similarity of adjacent voxels, the uncertainty of voxel values becomes large. Therefore *SD*, *ET* and *DV* increase, *UM* and *MI* become low with the decrease of X-ray dose level.

The correlation and similarity of adjacent voxels, which is evaluated by *EC* and *MIC*, become large in the filtered results returned by 3D AM. Therefore we can observe that the noises around the tumor are smoothed without blurring the tumor edge in the filtered results of 3D AM in comparison to those of 2D AM as shown in Figures 5 (c) and (d).

On the other hand, Matthieu et al. [20] reported that high-density objects generated radial streak-like artifacts in CT images. There exist radial artifacts from the bone region indicated by the white circle in Figure 1 where the density is high in the clinical images. The directions of these radial artifacts around the tumor indicated by an arrow in Figure 1 are almost parallel to the direction of *Y* axis. Therefore, the values of *EC(Y)* and *MIC(Y)* of the filtered result by using 3D AM are a little smaller than those obtained by 2D AM.

Although the adaptive median filter is extended from 2D to 3D, the *SD*, *ET*, *UM* and *DV* of results filtered by 3D AM and 2D AM are close. The quantum noise should be reduced more effectively without compromising the diagnostic image quality. Therefore, adaptive local averaging strategy is introduced into 3D AM to improve the image quality of low dose MDCT images. In Tables 1 and 2, 3D AMLA gives closer *ET* to the normal ones than 3D AM and 2D AM. It indicates that the distribution of voxel values of 3D AMLA is closer to that of normal-dose images. In addition, *EC* and *MIC* of 3D AMLA show the

similar tendency, which means that the distribution of the correlations and similarities of adjacent voxel values of 3D AMLA is closer to the normal ones. Finally, 3D AMLA improves effectively low-dose image quality because of similar image features to normal-dose images.

5. CONCLUSIONS

In this paper, the implementation of 2D AM, 3D AM and 3D AMLA filtering schemes and their application to 3D clinical low-dose MDCT data are described in detail. Local histograms and voxel value profiles are used to evaluate the filtering performance qualitatively. To evaluate the filtering efficiency quantitatively, several indices are applied to assessing the image quality in detail. Both qualitative and quantitative evaluating methods highlight the effective performance of 3D AMLA for reducing the quantum noise without the expense of the feature preservation. In addition, the proposed *EC* and *MIC* work well to assess the image quality in the directions of *X*, *Y* and *Z* axis precisely. A large reduction in the X-ray dose level of 3D abdominal MDCT images can be attained by applying 3D AMLA.

ACKNOWLEDGEMENTS

The authors would like to thank Mr. Toshihide Itoh (Chief Scientist of X-ray Computed Tomography, Siemens-Asahi Medical Technologies Ltd., Tokyo, Japan) for providing the low-dose MDCT datasets and giving us valuable comments.

REFERENCES

- [1] WD. Foley and U. Kerimoglu, "Abdominal MDCT: liver, pancreas, and biliary tract," *Seminars in ultrasound, CT, and MR*, Vol. 25, No. 2, pp. 122-144, 2004.
- [2] JE. Gray, "Safety (risk) of diagnostic radiology exposures". *Radiation risk: a primer*. Reston, VA: American College of Radiology, pp. 15-17, 1996.
- [3] K. Suzuki, I. Horiba, N. Sugie, and M. Nanki, "Neural filter with selection of input features and its application to image quality improvement of medical image sequences," *IEICE Trans. INF. & SYST.*, Vol. E85-D, No. 10, pp. 1710-1718, 2002.
- [4] Y. Funama, K. Awai, O. Miyazaki, T. Goto, Y. Nakayama, M. Shimamura, K. Hiraishi, S. Hori, and Y. Yamashita, "Radiation dose reduction in hepatic multidetector computed tomography with a novel adaptive noise reduction filter," *Radiat Med*, Vol. 26, No. 3, pp. 171-177, 2008.
- [5] Y. Funama, K. Awai, O. Miyazaki, Y. Nakayama, T. Goto, Y. Omi, T. Shimono, D. Liu, Y. Yamashita, and S. Hori, "Improvement of low-contrast detectability in low-dose hepatic multidetector computed tomography using a novel adaptive filter: evaluation with a computer-simulated liver including tumors," *Investigative Radiology*, Vol.41, No. 1, pp. 1-7, 2006.
- [6] A. C. Trægde Martinsen, H. Kjærnlie Sæther, D. R. Olsen, P. Skaane, and H. M. Olerud, "Reduction in dose from CT examinations of liver lesions with a new postprocessing filter: a ROC phantom study," *Acta Radiol*, Vol. 49, No. 3, pp. 303-309, 2008
- [7] M. Okumura, T. Ota, S. Tsukagoshi, and K. Katada, "New method of evaluating edge-preserving adaptive filters for computed tomography (CT): Digital phantom method," *Jpn. J. Radiol. Technol.*, Vol. 62, No. 7, pp. 971-979, 2006.
- [8] T. Sasaki, M. Sasaki, T. Hanari, H. Gakumazawa, Y. Noshi, and M. Okumura, "Improvement in image quality of non-contrast head images in multidetector-row CT by volume helical scanning with a three-dimensional denoising filter," *Radiat. Med.*, Vol. 25, No. 7, pp. 368-440, 2007.
- [9] T. Sasaki, T. Hanari, M. Sasaki, H. Oikawa, H. Gakumazawa, M. Okumura, Y.

- Ikeda, and N. Toyoshima, "Reduction of radiation exposure in CT perfusion study using a quantum de-noising filter," *Jpn. J. Radiol. Technol.*, Vol. 60, No. 12, pp. 1688-1693, 2004.
- [10] M. K. Kalra, M. M. Maher, D. V. Sahani, M. A. Blake, P. F. Hahn, G. B. Avinash, T. L. Toth, E. Halpern, and S. Saini, "Low-dose CT of the abdomen: evaluation of image improvement with use of noise reduction filters pilot study," *Radiology*, Vol. 228, No. 1, pp. 251-256, 2003.
- [11] M. K. Kalra, C. Wittram, M. M. Maher, A. Sharma, G. B. Avinash, K. Karau, T. L. Toth, E. Halpern, S. Saini, and J. A. Shepard, "Can noise reduction filters improve low-radiation-dose chest CT images? Pilot study," *Radiology*, Vol. 228, No. 1, pp. 257-264, 2003.
- [12] M. KachelrieB, O. Watzke, and W. A. Kalender, "Generalized multi-dimensional adaptive filtering for conventional and spiral single-slice, multi-slice, and cone-beam CT," *Med. Phys.* Vol. 28, No. 4, pp. 475-490, 2001.
- [13] Y.Q. Yang, N. Nakamori, and Y. Yoshida, "Improvement of cone beam CT image using singularity detection," *IEICE Trans. INF. & SYST.*, Vol. E86-D, No. 7, pp. 1206-1213, 2003.
- [14] N. Yasuda, Y. Ishikawa, and Y. Kodera, "Improvement of image quality in chest MDCT using nonlinear wavelet shrinkage with trimmed-thresholding," *Jpn. J. Radiol. Technol.*, Vol.61, No.12, pp. 1599-1569, 2005.
- [15] R. H. Chan, C. W. Ho, and M. Nikolova, "Salt-and-pepper noise removal by median-type noise detectors and detail-preserving regularization," *IEEE Trans. Image. Process.*, Vol. 14, No. 10, pp. 1479-1485, 2005.
- [16] Y. Zhang, R. Ning, D. Conover, and Y. Yu, "Image noise due to quantum fluctuations in flat-panel detector based cone-beam CT imaging," *Proceeding of SPIE*, Vol. 5754, No. 656, pp. 656-663, 2005.
- [17] Z. Wang and A.C. Bovik, "A universal image quality index," *IEEE Signal Processing Letters*, Vol. 9, No. 3, pp. 81-84, 2002.
- [18] Z. Wang, A.C. Bovik, H. R. Sheikh, and E. P. Simoncelli, "Image quality assessment: from error Visibility to structural similarity," *IEEE Transactions on Image Processing*, Vol. 13, No. 4, pp. 600-612, 2004.
- [19] C. Wang and K.L. Ma "A statistical approach to volume data quality assessment," *IEEE transaction on visualization and computer graphics*, Vol. 14, No. 3, pp. 590-602, 2008.
- [20] B. Matthieu, C. Hasan, S. Krishna, E. Kai, and S. Lothar, "A radial adaptive filter for metal artifact reduction," *Medical Imaging 2005: Image Processing*. Vol. 5747, pp. 2075-2082, 2005.

AUTHOR INFORMATION



Jiehang Deng received his M.E. degree in pattern recognition and intelligent system from Xian University of Technology, China, in 2005. From 2005 to 2006, he worked at Mindray Medical International Limited. Now he is working toward the doctor degree at the Graduate School of Engineering, University of Fukui. His main interest is in the field of medical image processing. He is a student member of JAMIT and IEICE.



Koichiro Hiratsuka received his M.E. degree from Fukui University, Japan, in 2002. He is currently a technical assistant at the Center for Computing and Network Services of the University of Fukui.

His main interest is in the field of medical image processing.



Tomokazu Ishida completed the Radiological Technology course at Fujita Health University in 1995. Currently, he is a radiological technologist in University of Fukui Hospital. His main interest is in image processing of CT

and MRI images, especially improvement of low contrast resolution and image noise with low dose CT examination.



Haruhiko Shirai was a member of the technical staff at the Department of Information Science, Faculty of Engineering, University of Fukui, Japan. He is currently a member of technical staff at the Technical Support Division, Faculty of Engineering, University of Fukui. He received his Ph.D. in Engineering from the University of Fukui in 2006. His main research field is computer user authentication based on the user model.



Jousuke Kuroiwa received his Ph.D. in engineering from Tohoku University in 1996. He was a member of the technical staff at Department of Electrical Communication Engineering, Tohoku University until 1997, and with the Division of

Mathematical and Information Sciences, Hiroshima University until 2002. He is now an associate professor engaging in research on nonlinear dynamics and dynamical neural computations in the Department of Human and Artificial Intelligent Systems, University of Fukui. He is a member of IEICE, IPSJ, JNNS, and PSJ.



Tomohiro Odaka received his Ph.D. in Engineering from Waseda University, Japan, in 1990. He is a professor at the Graduate Program of Nuclear Power and Energy Safety Engineering,

Graduate School of Engineering, University of Fukui Graduate School, Japan. He is a member of IEEE CS, ACM, IPSJ, IEICE, JSMBE, and AESJ. His research activities focus on user modeling, network security, biomedical signal processing, intelligent human interface, and computer aided instruction.



Hisakazu Ogura received his Ph.D. in science from Kyoto University, Japan, in 1977. He is currently a professor at the Department of Human and Artificial Intelligence Systems at the Faculty of

Engineering, University of Fukui, Japan. His main interests and research activities are in knowledge representation and processing in the fields of artificial intelligence, medical informatics and medical image processing by applying genetic algorithms, artificial neural networks, symbol processing and fuzzy theory. He is a member of IECE, IPSJ and SOFT Japan.